

On the Viability of Using Autonomous Three-Component Nodal Geophones to Calculate Teleseismic P_s Receiver Functions with an Application to Old Faithful, Yellowstone

by Kevin M. Ward and Fan-Chi Lin

ABSTRACT

Recent advances in seismic data-acquisition technology paired with an increasing interest from the academic passive source seismological community have opened up new scientific targets and imaging possibilities, often referred to as Large-N experiments (large number of instruments). The success of these and other deployments has motivated individual researchers, as well as the larger seismological community, to invest in the next generation of nodal geophones. Although the new instruments have battery life and bandwidth limitations compared to broadband instruments, the relatively low deployment and procurement cost of these new nodal geophones provides an additional novel tool for researchers. Here, we explore the viability of using autonomous three-component nodal geophones to calculate teleseismic P_s receiver functions by comparison of co-located broadband stations and highlight some potential advantages with a dense nodal array deployed around the Upper Geyser basin in Yellowstone National Park. Two key findings from this example include (1) very dense nodal arrays can be used to image small-scale features in the shallow crust that typical broadband station spacing would alias, and (2) nodal arrays with a larger footprint could be used to image deeper features with greater or equal detail as typical broadband deployments but at a reduced deployment cost.

INTRODUCTION

Converted wave imaging using the receiver function method (Langston, 1979) is a common technique employed by seismologists to investigate Earth structure over a wide range of spatial scales and tectonic environments. For example, individual station analysis can provide information about the thickness of the crust and bulk crustal V_p/V_s ratios (e.g., Zhu and Kanamori, 2000; Beck and Zandt, 2002). Using the common conversion-point stacking method (Duker and Sheehan, 1997), receiver function analysis across seismic arrays enhances overlapping sensitivity to common structures at depth and can recover subtler features of the Earth (e.g., Schmandt *et al.*, 2012).

Combining receiver functions with surface waves into a joint seismic inversion (Julià *et al.*, 2000) has helped ameliorate the inherent nonuniqueness of inverting receiver functions for velocity structures (Ammon *et al.*, 1990) and has opened up new tomography possibilities in crustal imaging (e.g., Shen *et al.*, 2013; Ward *et al.*, 2014). The aforementioned examples represent a select (nonexhaustive) assortment of possible applications highlighting the increasing utility, versatility, and popularity of the receiver function method in seismic imaging.

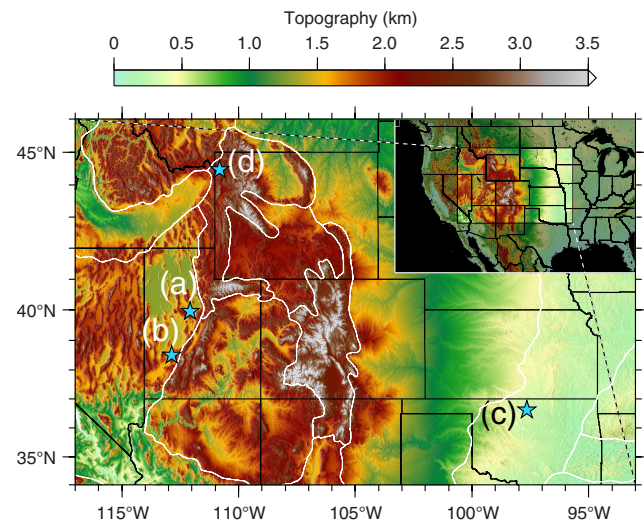
Traditionally, broadband seismic instruments have been used in many of these receiver function studies (Frassetto *et al.*, 2010), with relatively few examples of researchers incorporating short-period instruments (~ 1 Hz corner frequency) into their analysis (e.g., Yuan *et al.*, 1997; Jones and Phinney, 1998; Zhu, 2000; Niu *et al.*, 2005; Wölbern *et al.*, 2009; Delph *et al.*, 2017). Recently, the academic passive source seismological community has begun to explore the use of dense nodal geophone deployments in response to increasing instrument technology and availability. Prominent examples of Large-N (large number of instruments) experiments include the Long Beach Array in southern California (Lin *et al.*, 2013) and the Imaging Magma Under St. Helens (iMUSH) experiment in southern Washington (Hansen and Schmandt, 2015), with the arrays consisting of over 5000 and 900 one-component 10-Hz nodal geophones, respectively. The increasing interest in Large-N deployments was recently highlighted by the Community Wavefield Experiment in Oklahoma (Anderson *et al.*, 2016), which deployed ~ 370 of the newly available three-component 5-Hz nodal geophones in northern Oklahoma. Using one-component nodal geophones (10 Hz corner frequency), teleseismic body waves, earthquake relocations, and ambient noise tomography methods have been applied to image, in unprecedented detail, upper mantle (Inbal *et al.*, 2016), crustal (Schmandt and Clayton, 2013), and upper crustal (Lin *et al.*, 2013) Earth structures. Because of the relatively low procurement cost, several primary investigators at research institutions have purchased autonomous three-component nodal geophones and

have them immediately available for individual deployments as well as integration into larger multi-institution deployments.

The focus of this study is to demonstrate the viability of using newly available autonomous three-component nodal geophones (also referred to as high-frequency sensors or nodes) to calculate teleseismic P_s receiver functions. Specifically, we use FairfieldNodal Zland 3C nodal geophones (5 Hz corner frequency) that have a variable sampling interval (up to 0.5 ms) and can operate autonomously for up to ~ 40 days. Although we focus on one specific application in this study (teleseismic P_s receiver functions), we emphasize that these specific three-component nodal geophones might be utilized in other receiver function applications not explored in this study (e.g., S_p , local events, and joint inversions). Depending on the scientific target, nodal geophones may provide several advantages over traditional broadband-only deployments, including reduced deployment time and costs. The reduced capital required for deployments consisting of nodal geophones can thus be diverted to densifying a selected region or expanding the footprint of an array over a larger area (Large-N); deployment configurations that have typically been under the purview of industry-scale, controlled-source seismology. With the increasing availability of nodal geophones to individual researchers and the successful demonstration that nodal geophones are a viable instrument for receiver function studies, numerous scientific targets can be investigated at reduced costs or in expanded detail.

DATA AND METHODS

In this study, we use broadband seismic data collected by The University of Utah Seismograph Stations (UU) permanent network (University of Utah, 1962) and the Incorporated Research Institutions for Seismology (IRIS) Community Wavefield Experiment in Oklahoma (YW) temporary network (Anderson *et al.*, 2016) for comparison with the waveforms recorded by temporary nodal geophones at three separate locations. An additional fourth location is presented here for which we highlight the application of receiver function imaging across a small-scale dense array of nodal geophones (Fig. 1). Specifically, the UU broadband stations NLU (North Lily, Utah), FOR2 (Blundell East, Utah), and the YW broadband station 513 (Hunter, Oklahoma) were chosen for this study because of their close proximity to deployed nodal geophones (collocated to near-collocated). With the specific target of evaluating the nodal geophones' ability to reproduce receiver functions calculated from a collocated broadband station, we deployed eight temporary nodal instruments in early 2016 (22 January–19 February) near the permanent UU broadband station NLU (Fig. 2a). As part of the Frontier Observatory for Research in Geothermal Energy (FORGE) project, the University of Utah deployed 93 nodal geophones during the winter of 2016/2017 (14 December 2016–14 January 2017) in a larger gridded geometry (Fig. 2b). Of those 93 nodal stations, station 12s was deployed within 300 m of the permanent UU broadband station FOR2 and is used in this study. We also use data

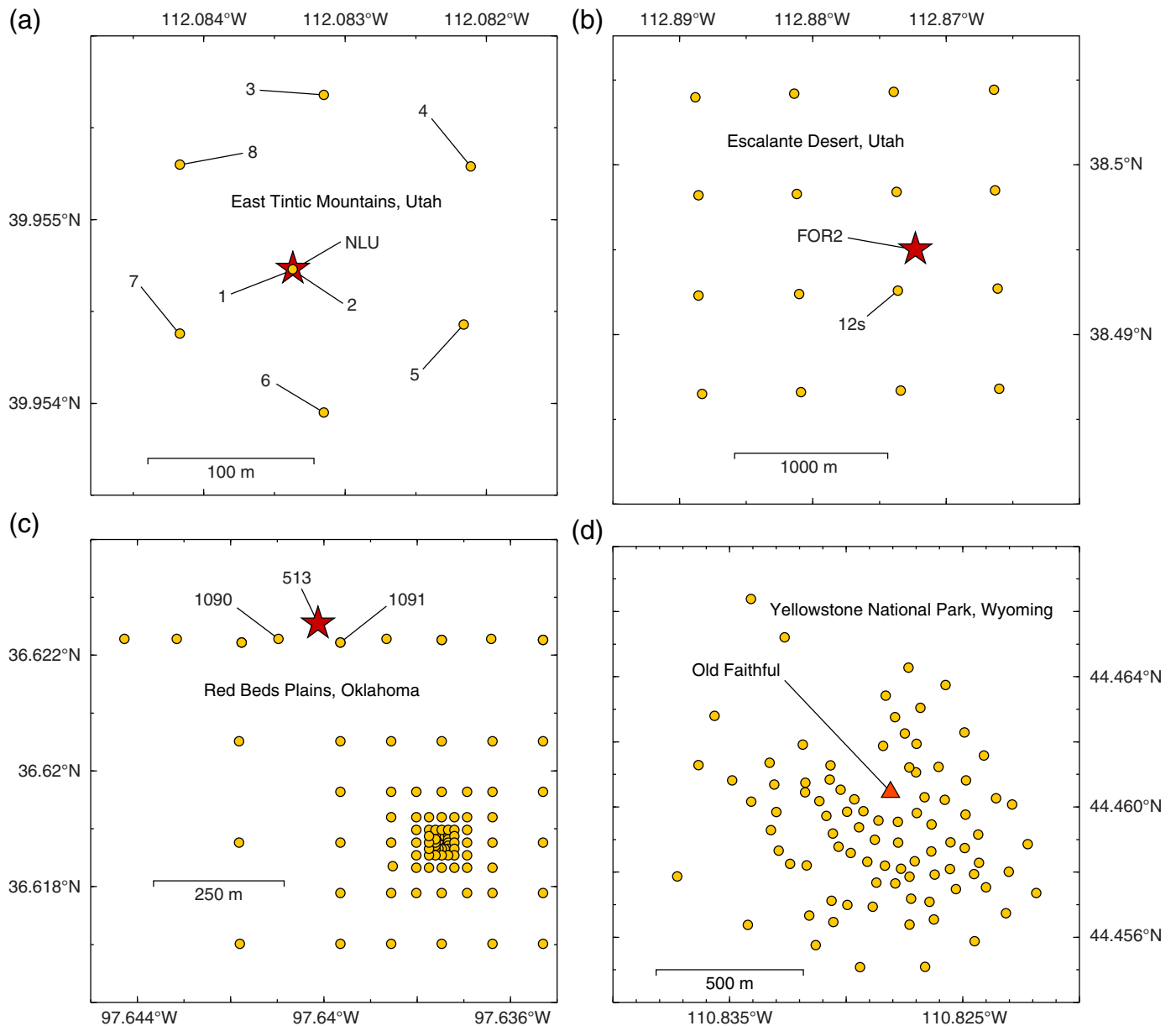


▲ **Figure 1.** Location map showing the four nodal deployment sites (blue stars) used in this study, with major physiographic provinces delineated by lines: (a) East Tintic Mountains, Utah; (b) Escalante Desert, Utah; (c) Red Beds Plains, Oklahoma; and (d) Old Faithful, Yellowstone National Park, Wyoming. The color version of this figure is available only in the electronic edition.

collected in 2016 (24 June–21 July) by the IRIS Community Wavefield Experiment in Oklahoma in which the YW broadband station 513 and closely located (< 50 m) nodal stations 1090 and 1091 were contemporaneously deployed (Fig. 2c).

Finally, we provide an additional application of three-component nodal geophones deployed around the Old Faithful Geyser in Yellowstone National Park to highlight the small-scale features observable with a dense array (Fig. 2d). The data used in this example were collected in November 2015 (2 November 2015–14 November 2015). Although the deployment duration was short (~ 12 days) and few teleseismic events were recorded by the array, one event yielded high-quality receiver functions. In this deployment (Old Faithful, Yellowstone National Park) along with the FORGE and NLU nodal geophone deployments, we use a linear phase antialiasing filter with an 18 dB gain during data acquisition. The comparability of specific receiver function features recovered at each location presented here could have been presented from only one location. However, the use of multiple geographic locations within at least three distinct tectonic regimes (a stable continental interior, active basin and range, and an active hotspot and hydrothermal system) and two distinct site geologies (near-surface bedrock vs. thick sediments) strengthens our contention that autonomous three-component nodal geophones are viable instruments for use in receiver function analysis.

The criteria for events used in typical teleseismic receiver function studies vary depending on the scientific target and geographic location but often include an initial search for events with an $M_w > 5.5$ and an epicentral distance between 30° and 95° . We note that the events selected for use in this

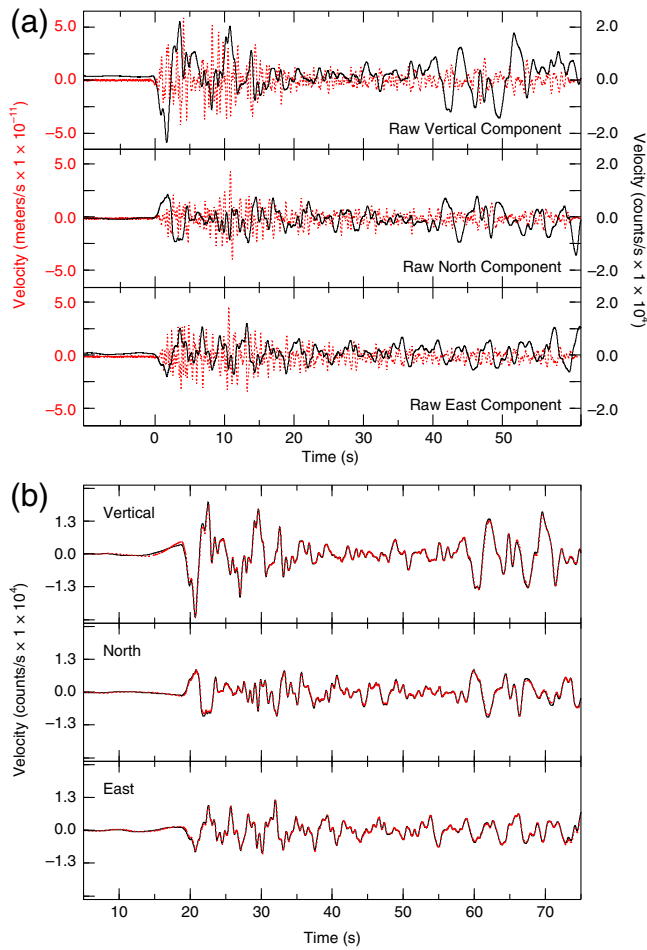


▲ **Figure 2.** (a–d) Specific station deployment geometries for each of the four locations referenced in Figure 1 and in the text. Broadband stations are shown as stars, and three-component nodal geophones are shown as circles. Stations used in this study are labeled with their station names in each of the subplots. The color version of this figure is available only in the electronic edition.

study are intended to be demonstrative and not exhaustive in reproducing every teleseismic P_s receiver function possible for the four deployments. Therefore, we present results from a range of event magnitudes (M_w 5.9–7.6), event depths (12–163 km), and epicentral distances (39° – 89°) that highlight the scope over which nodal geophones can reproduce receiver functions generated at nearby broadband stations. We also vary the corner frequencies of the band-pass filter described in the following section to further show the similarity of receiver functions calculated from nodal geophones and broadband stations.

Initial processing of the raw waveforms varies slightly, based on the instrument recording the teleseismic event

(e.g., broadband vs. nodal geophone), but the data preprocessing is similar and described here. Common to all instruments, the waveforms are windowed around the theoretical teleseismic P arrival (-20 to 80 s) and then decimated to 50 samples per second using an impulse response filter to prevent aliasing (Fig. 3a). After decimation, the mean and trend are removed, and a Hanning taper is applied. At this stage in the preprocessing, the instrument response is removed from the nodal instruments, resulting in a time series with units of displacement. Removing the instrument response from the nodal instruments (5 Hz corner frequency) helps recover a relatively broad frequency band and has been demonstrated to generate robust receiver functions in other studies using different short-period



▲ **Figure 3.** (a) Comparison of raw waveform components for event 2016/01/30 03:25:10 (Table 1) from both a broadband station (NLU, solid waveforms) and a collocated nodal geophone (1, dotted waveforms). (b) Comparison of the same broadband and nodal geophone data after the instrument response has been removed from the nodal geophone data, and a band-pass filter (0.1–4.0 Hz) has been applied to all waveforms. The color version of this figure is available only in the electronic edition.

(~ 1 Hz corner frequency) instruments (e.g., Jones and Phinney, 1998; Niu *et al.*, 2005; Wölber *et al.*, 2009; Delph *et al.*, 2017). To facilitate a direct comparison of the processed broadband and nodal geophone waveforms, we take the derivative of the nodal data, thus converting them to units of velocity (Fig. 3b). A Butterworth filter with four poles and two passes is then applied to all waveforms, and the horizontal components are rotated into the earthquake radial and tangential coordinate system.

In this study, we employ the time-domain iterative deconvolution method (Ligorria and Ammon, 1999) to estimate receiver functions but note that other single-station methods, such as the frequency-domain water-level-stabilized method (e.g., Clayton and Wiggins, 1976), array-based deconvolution methods (e.g., Neal and Pavlis, 1999; Chen *et al.*, 2010), or more sophisticated transdimensional hierarchical Bayesian ap-

proaches (Kolb and Lekić, 2014) might be equally appropriate. The time-domain iterative deconvolution method used here begins by cross correlating the vertical component with the horizontal component (radial for radial receiver functions and tangential for tangential receiver functions) to estimate the time lag of the largest spike. This initial receiver function estimate (single-spike Green's function) is convolved with the vertical component and subtracted from the horizontal component. The process is iteratively updated, producing a spike train that minimizes the difference between the predicted (receiver function estimate convolved with the vertical component) and observed horizontal component, providing a quantitative, albeit arbitrary, misfit threshold.

The final Green's function estimate $f(t)$ is convolved with a low-pass Gaussian filter $g(t)$ such that our receiver functions $r(t)$ have the following form in the time domain (t):

$$r(t) = f(t) * g(t). \quad (1)$$

The Gaussian filter $g(t)$ acts to mitigate high-frequency noise and has the form:

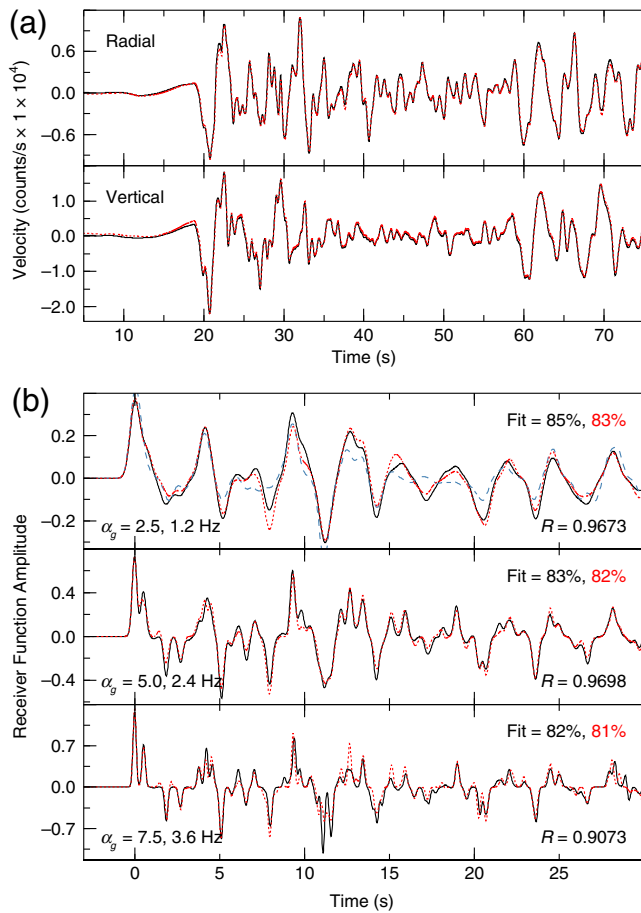
$$g(t) = e^{-\alpha_g^2 t^2}. \quad (2)$$

Larger α_g values produce smaller pulse widths (higher frequency content), resulting in a trade-off between vertical resolution of structures and potential artifacts from noisy data. The value of α_g depends on the specific scientific target being investigated, but an α_g value of 2.5 (~ 1.2 Hz) is common for crustal-scale teleseismic P_s receiver function studies (e.g., Gans *et al.*, 2011; Stanciu *et al.*, 2016).

RESULTS AND DISCUSSION

Our results are organized into four geographic locations (Fig. 1), with the first three locations highlighting a specific receiver function feature recovered by the nodal geophones and nearby broadband station. The first location (East Tintic Mountains, Utah; Fig. 2a) shows a comparison of radial and transverse receiver functions for a single collocated nodal station, along with a comparison of radial receiver functions for seven other nearby (< 100 m) nodal stations. The second location (Escalante Desert, Utah; Fig. 2b) shows a comparison of radial receiver functions for two separate events recorded at the same broadband–nodal station pair. The third location (Red Beds Plains, Oklahoma; Fig. 2c) shows a comparison of radial receiver functions generated from the same event recorded at two distinct broadband–nodal station pairs. The final location (Yellowstone National Park, Wyoming; Fig. 2d) highlights shallow small-scale features observable with a dense nodal array and a deeper large-scale feature, consistent with previous work.

When available from the EarthScope Automated Receiver Survey (EARS), an IRIS data product (Crotwell and Owens, 2005; IRIS Data Management Center [DMC], 2010; Trabandt *et al.*, 2012), equivalent receiver function results are plotted with dashed lines. Subtle differences are observed between



▲ **Figure 4.** (a) Vertical and radial components for event 2016/01/30 03:25:10 (Table 1), preprocessed as described in the text (band-pass filter 0.1–4.0 Hz), with broadband data (NLU) shown as solid lines and nodal geophone data (1) shown as dotted lines. (b) Radial receiver function results for three α_g values (2.5, 5.0, and 7.5), with the receiver function fit (shown in the upper right of each subplot) and correlation coefficients (R value shown in the lower right of each subplot) between broadband and nodal geophone results. For comparison, the radial receiver function from the EarthScope Automated Receiver Survey (EARS) is shown as a dashed line for the α_g value of 2.5. The color version of this figure is available only in the electronic edition.

the receiver functions generated from the EARS catalog and receiver functions calculated in this study. We attribute this variation to differences in the preprocessing of the raw waveform data (e.g., the time window used in deconvolution and band-pass filter corners) but note that the receiver functions calculated for the same broadband stations are extremely similar. A more important comparison is the similarity of the receiver functions calculated from nodal geophones and broadband stations. Beyond a qualitative visual inspection of the receiver functions similarity, we quantify the similarity of each (nodal geophone)–(broadband receiver function) result by calculating the correlation coefficients for comparison (in which 0 corresponds to no correlation, and 1 represents a direct correlation). Finally, the fit of the receiver function to the data (fit is discussed in the previous section) is included in the plots as well. For the purposes of this study, the absolute fit is not as important as the relative fit between the nodal geophones and broadband receiver functions.

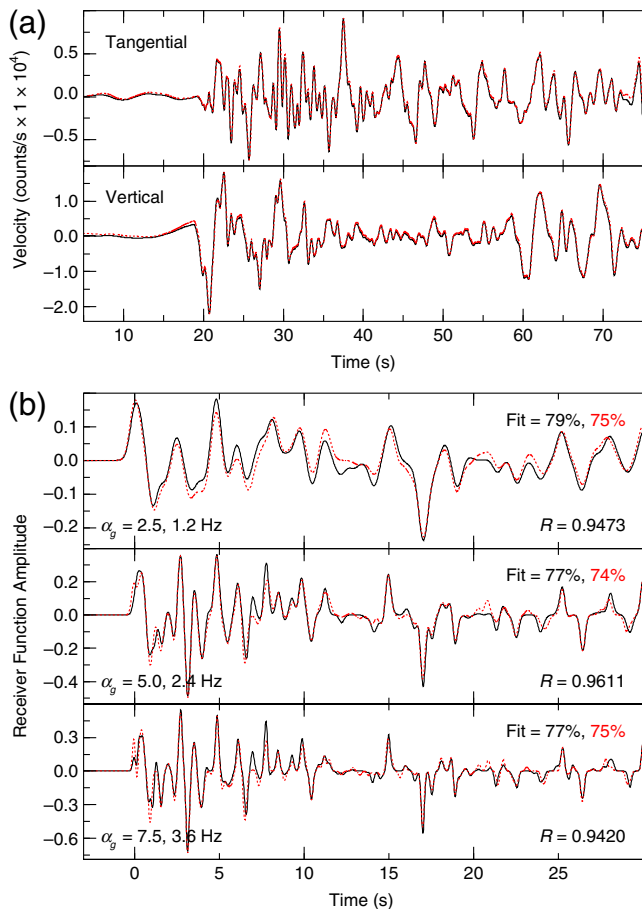
East Tintic Mountains, Utah (NLU)

In total, we deployed eight nodal geophones near (<100 m) the permanent UU network station NLU. Station 1 was collocated with NLU (on the same concrete pad as the broadband instrument), and the other seven geophones were deployed in a ring (Fig. 2a) around NLU (spiked into the ground on the surface). The event used at this location is an intermediate-depth subduction-zone earthquake (Table 1) and with a broad band-pass filter (0.1–4 Hz) applied to the processed horizontal and vertical waveforms (Figs. 4a and 5a). The 4 Hz corner allows receiver functions with higher frequency content (1.2, 2.4, and 3.6 Hz) to be calculated using three separate α_g values (2.5, 5.0, and 7.5). It is not surprising that the radial and tangential receiver functions (Figs. 4b and 5b) have high correlation coefficients (> 0.94 for α_g values of 2.5) when inspecting the similarity of the data (Figs. 4a and 5a) used to calculate them. It is noteworthy that all of the geophones recovered similar receiver functions (Fig. 6), regardless of whether the instrument was deployed on a concrete pad (station 1; Fig. 2a) or spiked into the ground (stations 3–8; Fig. 2a). Although it is beyond the scope of this study to geologically interpret the individual receiver functions at this location, we observe a solid positive arrival around 4 s (Fig. 4a) that is consistent with previous

Table 1
Event Data Used in This Study

Time (yyyy/mm/dd hh:mm:ss)	Latitude (°)	Longitude (°)	Depth (km)	Magnitude	Back Azimuth (°)	Distance (°)	BB/SP Station Pair
2016/01/30 03:25:10	54.0057	158.5128	163	7.2	316.25	58.6025	NLU/1–8
2016/12/25 14:22:27	–43.4053	–73.9403	38	7.6	152.737	88.8295	FOR2/12s
2016/12/21 16:43:57	21.5036	145.417	12	5.9	293.85	85.5498	FOR2/12s
2016/07/11 02:01:09	0.5874	–79.6358	17	5.9	150.958	39.5464	513/1090–1091
2015/11/09 16:10:28	51.6394	–173.075	15	6.5	302.959	41.0876	n/a

BB, broadband; SP, short period.

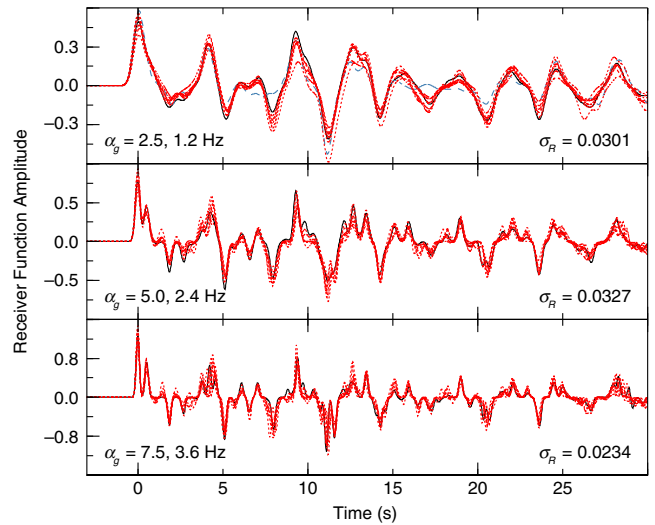


▲ **Figure 5.** (a) Vertical and tangential components for event 2016/01/30 03:25:10 (Table 1), preprocessed as described in the text (band-pass filter 0.1–4.0 Hz), with broadband data (NLU) shown as solid lines and nodal geophone data (1) shown as dotted lines. (b) Tangential receiver function results for three α_g values (2.5, 5.0, and 7.5), with the receiver function fit (shown in the upper right of each subplot) and correlation coefficients (R value shown in the lower right of each subplot) between broadband and nodal geophone results. The color version of this figure is available only in the electronic edition.

estimates of the Moho P_s arrival at this location (Crotwell and Owens, 2005; IRIS-DMC, 2010; Trabant *et al.*, 2012).

Escalante Desert, Utah (FOR2)

Related to the FORGE project, 93 nodal stations were deployed in the Escalante Desert (Great Basin) as part of the Enhanced Geothermal System Testing and Development at the Milford, Utah, FORGE Site experiment. A nodal station was deployed near (<300 m) the permanent UU network station FOR2 (Fig. 2b) and was available for use in this study. For this location, two shallow subduction-zone events with different magnitudes and back azimuths (Table 1) were used. A slightly narrower band-pass filter (0.1–2.5 Hz) was applied to the processed radial and vertical waveforms (Figs. 7a and 8a). High correlation coefficients (>0.93 for α_g values of 2.5) are also

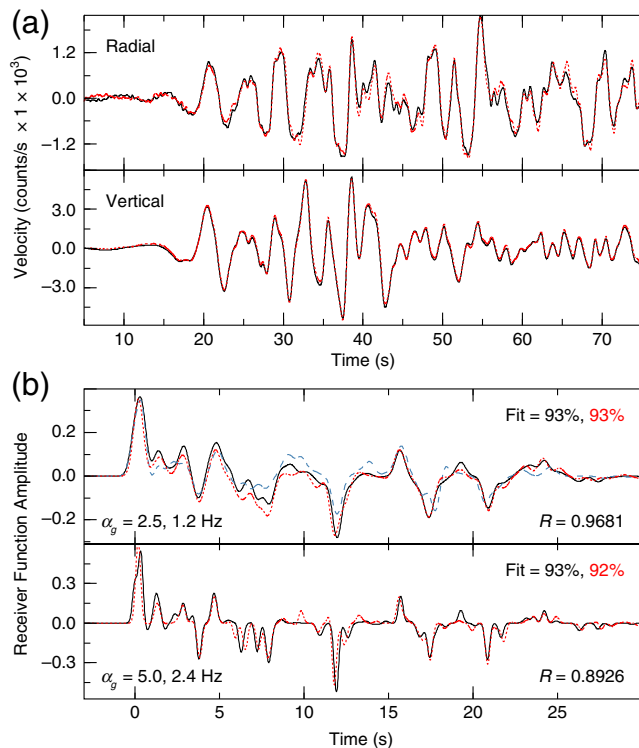


▲ **Figure 6.** Radial receiver function results for event 2016/01/30 03:25:10 (Table 1). Nodal geophone stations 1–8 (dotted lines) located near the broadband station NLU (solid lines) are shown for three α_g values (2.5, 5.0, and 7.5). The standard deviation of the correlation coefficients between the broadband station and each nodal geophone result is shown in the lower right of each subplot. For comparison, the radial receiver function from the EARS is shown as a dashed line for the α_g value of 2.5. The color version of this figure is available only in the electronic edition.

observed between the nodal geophones and broadband receiver functions (Figs. 7b and 8b). Although the two events have different rupture properties, radiation patterns, and travel paths to the stations (visible in the radial and vertical components), similar arrivals can be identified in the radial receiver functions. At around 2.5 s, we observe a strong midcrustal arrival, and around 4.5 s, an arrival consistent with previous estimates of the Moho depth in this area is visible in both events (Crotwell and Owens, 2005; IRIS-DMC, 2010; Trabant *et al.*, 2012).

Red Beds Plains, Oklahoma (513)

The IRIS Community Wavefield Experiment in Oklahoma occupied 370 locations with three-component nodal geophones in three dense lines and one 7-layer nested gradiometer configuration. For the purpose of this study, data from two nodal geophones (located within 50 m of station 513) and one broadband station available from the IRIS-DMC are used here (Fig. 2c). The event used in this location is a shallow subduction-zone event with the closest epicentral distance and lowest magnitude used in this study (Table 1). A relatively narrow band-pass filter (0.2–1.5 Hz) is applied to the processed radial and vertical waveforms (Fig. 9a). High-correlation coefficients (>0.93 for α_g values of 2.5) are observed at both station locations (Fig. 9b), with a significantly more-complicated shallow subsurface structure compared to the two Utah sites indicated in the radial receiver function results. An arrival around 5.5 s is consistent with the Moho depth estimates in this area (Crotwell and Owens, 2005; IRIS-DMC, 2010; Trabant *et al.*,



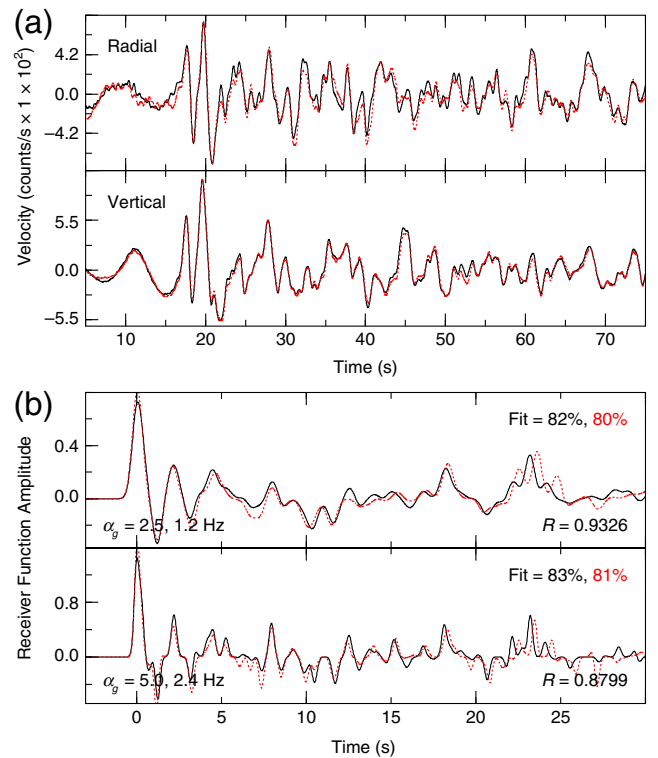
▲ **Figure 7.** (a) Vertical and radial components for event 2016/12/25 14:22:27 (Table 1), preprocessed as described in the text (band-pass filter 0.1–2.5 Hz), with broadband data (FOR2) shown as solid lines and nodal geophone data (12s) shown as dotted lines. (b) Radial receiver function results for two α_g values (2.5 and 5.0), with the receiver function fit (shown in the upper right of each subplot) and correlation coefficients (R value shown in the lower right of each subplot) between broadband and nodal geophone results. For comparison, the radial receiver function from the EARS is shown as a dashed line for the α_g value of 2.5. The color version of this figure is available only in the electronic edition.

2012), and a shifted coherence peak around 0.5 s suggests a complicated shallow (< 2 km) structure consistent with a thick sediment package at this location.

Old Faithful, Yellowstone National Park, Wyoming

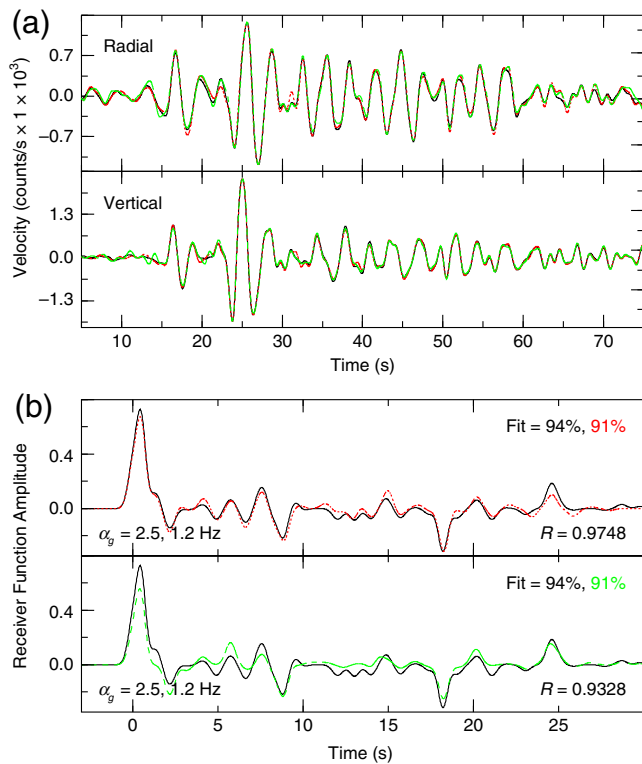
An exceptionally dense array of three-component nodal geophones was deployed around the Old Faithful Geyser in November 2015. Although the deployment was limited to 12 days, we were able to use one shallow subduction-zone event (Table 1) with a broad band-pass filter (0.1–8 Hz). The 8 Hz corner allows receiver functions with higher frequency content to be extracted and shallower structures (< 7 km) investigated. For the radial receiver functions shown in this case, we use an α_g value of 10 (~ 4.8 Hz). In Figure 10a, we plot the time lag of the first positive arrival after zero at each station across the array.

Our radial receiver function results show considerable small-scale variability (< 50 m) in the shallow uppermost crust beneath the Upper Geyser basin (Fig. 10a). This is not unex-



▲ **Figure 8.** (a) Vertical and radial components for event 2016/12/21 16:43:57 (Table 1), preprocessed as described in the text (band-pass filter 0.1–2.5 Hz), with broadband data (FOR2) shown as solid lines and nodal geophone data (12s) shown as dotted lines. (b) Radial receiver function results for two α_g values (2.5 and 5.0), with the receiver function fit (shown in the upper right of each subplot) and correlation coefficients (R value shown in the lower right of each subplot) between broadband and nodal geophone results. The color version of this figure is available only in the electronic edition.

pected, given the variable hydrothermal features observed on the surface. It should be noted that at these small arrival times, differences in topography (i.e., station elevation and path length) need to be addressed when interpreting the results. A simple linear regression fit between the time lag plotted in Figure 10a and the elevation of the station has an R^2 value of 0.006, suggesting that topographic differences are not generating the patterns observed in our results. Furthermore, if the arrival-time lags in Figure 10a were an artifact of noise in the data, we would expect a random distribution and not the coherent grouping we observe. Finally, the largest-amplitude negative arrival has an average time lag of 0.82 ± 0.04 s across the entire array, is relatively flat compared with the first positive arrival, and corresponds to the top of a large upper-crustal magma reservoir (~ 6 km LVZ) seen in other studies (e.g., Chu *et al.*, 2010; Huang *et al.*, 2015). With only one event, it is typically difficult to establish the robustness of any receiver function result. However, for the reasons discussed above, we are confident enough to interpret the shallow-structure results, albeit in a qualitative sense.



▲ **Figure 9.** (a) Vertical and radial components for event 2016/07/11 02:01:09 (Table 1), preprocessed as described in the text (band-pass filter 0.2–1.5 Hz), with broadband data (513) shown as solid lines, nodal geophone data (1090) shown as dotted lines, and nodal geophone data (1091) shown as dashed lines. (b) Radial receiver function results for one α_γ value (2.5), with the receiver function fit (shown in the upper right of each subplot) and correlation coefficients (R value shown in the lower right of each subplot) between broadband and nodal geophone 1090 (dotted lines) and 1091 (dashed lines). The color version of this figure is available only in the electronic edition.

Despite the considerable small-scale variability observed in Figure 10a, a close examination of the waveforms reveals most of the receiver functions fall into one of two groups: those with two arrivals within the first second (Fig. 10b, top) and those with three arrivals within the first second (Fig. 10b, bottom). The first group (with two arrivals) are plotted with circles in Figure 10a. The six locations in the second group (with three arrivals) are plotted with squares in Figure 10a. A few locations are plotted with diamonds and show a hint of a negative first arrival but are placed into the first group with two arrivals because of the similarity to other receiver functions in that group. The spatial distribution of the diamonds is especially interesting because it marks the transition between the two groups to the north and east of the second group (Fig. 10a, squares). To the south and west of the second group (Fig. 10a, squares), the boundary is sharp, meaning that the first arrivals are clearly positive in the receiver functions to the south and west of the second group.

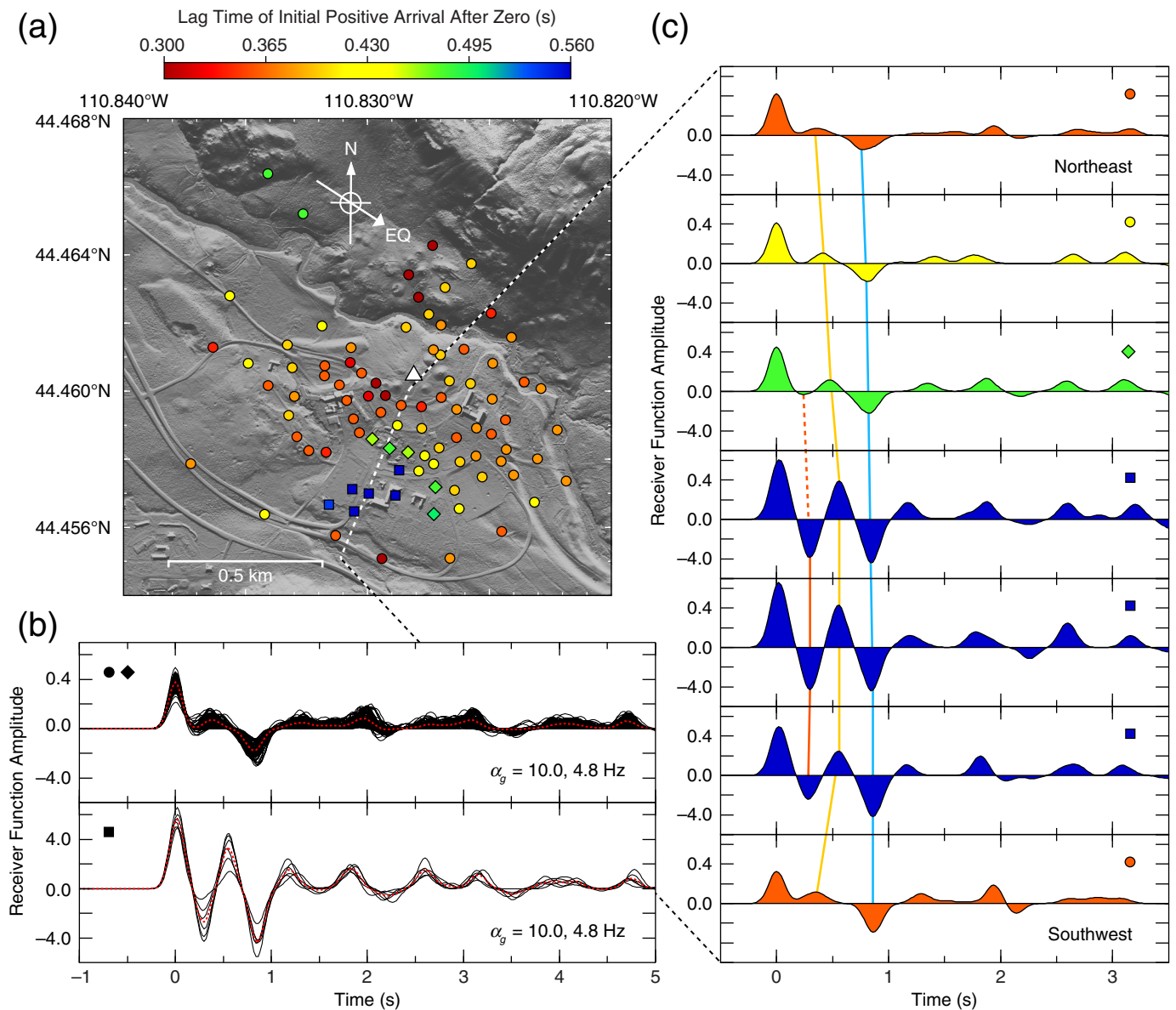
We interpret the first negative arrival (~ 0.26 s) in the second group (Fig. 10a, squares) as the top of a shallow

low-velocity layer that has a sharp southern and western boundary but a more gradational northern and eastern boundary (Fig. 10c). Placing depth constraints on these layers is currently untenable, because a sufficiently complex shallow velocity model does not yet exist for this area. However, projecting the piercing points of these interfaces along the back azimuth of the earthquake ($\sim 300^\circ$) shifts the location of our interpreted low-velocity zone to the southwest of the Old Faithful Geyser. It is noteworthy that recent work by S. Wu *et al.* (unpublished manuscript, 2017; see [Data and Resources](#)) also images a shallow (< 60 m) low-velocity feature in the same general area of our shallow (but still deeper) low-velocity zone. We suggest our low-velocity zone might be the deeper signature of heat or hydrothermal fluids that ultimately source or drive the Upper Geyser basin hydrothermal system.

CONCLUSIONS

In this study, we used nodal geophones closely located to broadband instruments in three separate geographic locations to investigate the viability of using autonomous three-component nodal geophones to calculate teleseismic P_s receiver functions. An additional application to the Old Faithful area in Yellowstone National Park was included to highlight the potential utility of a dense nodal array for receiver function analysis. Across three tectonic regimes, two site geologies, and multiple event characteristics (including magnitude, depth, and epicentral distance, along with four different preprocessing band-pass filters) we demonstrated that nodal geophones are capable of reproducing receiver functions with high fidelity. With a more targeted deployment, the Yellowstone example highlights two exciting possible applications of nodal arrays in the context of receiver function analysis: (1) Very dense arrays can be used to image small-scale features of the shallow crust that typical broadband station spacing would alias; (2) Nodal arrays with a larger footprint could be used to image deeper features (i.e., the top of magma reservoir in our Old Faithful example) with greater or equal detail as typical broadband stations but at a reduced deployment cost.

Currently, the deployment time of nodal geophones is limited by their battery life (< 40 days) and, depending on the scientific target, this may limit the range and applications of specific receiver function studies. However, recent short-duration rapid deployments (~ 1.5 months) of broadband stations using the receiver function method (and other imaging techniques, such as surface-wave tomography) have yielded useful Earth velocity and structural information (e.g., [Ma and Clayton, 2016](#)). The results of these short-duration rapid deployments can then be used to direct future deployments or utilize new processing methods (e.g., [Kolb and Lekić, 2014](#)) to investigate Earth structure in unprecedented detail. Future receiver function studies are planned that will exploit the low-cost rapid deployment of dense station configurations afforded by the new autonomous three-component nodal geophones.




▲ **Figure 10.** (a) Nodal geophones deployed around the Old Faithful Geyser (triangle) in Yellowstone National Park. Shapes correspond to the time lag of the first positive arrival for event 2015/11/09 16:10:28 (Table 1). (b) All radial receiver functions (solid lines) sorted and stacked (dotted lines) into two groups from this array and event where receiver functions (top) with two arrivals within the first second and (bottom) those with three arrivals within the first second are grouped together. The first group (with two arrivals) plots as circles in (a). The six locations in the second group (with three arrivals) plot as squares in (a). (c) Seven radial receiver functions plotted along the north-southwest dashed white line in (a). Three lines connect three distinct arrivals found in the first second of each receiver function along the line. The color version of this figure is available only in the electronic edition.

DATA AND RESOURCES

Seismograms used in this study were obtained from the Incorporated Research Institutions for Seismology (IRIS) Data Management Center at www.iris.edu (last accessed February 2017), as well as those collected by the University of Utah. Metadata for The University of Utah Seismograph Stations (UU) permanent network and temporary Community Wavefield Experiment in Oklahoma (YW) can be found at <http://ds.iris.edu/mda/UU> and <http://ds.iris.edu/mda/YW/>

[timewindow=2016-2016](#) (both last accessed February 2017). Event origin times and locations are taken from the National Earthquake Information Center–Preliminary Determination of Epicenter (NEIC-PDE) catalog U.S. Geological Survey, <http://earthquake.usgs.gov/data/pde.php> (last accessed February 2017). The digital elevation model (DEM) in Figure 10a was downloaded from <http://opentopo.sdsc.edu/raster?jobId=rt1485139073565> (last accessed May 2017). The unpublished manuscript by S. Wu, K. M. Ward, F. Lin, J. Farrell, M. Karplus, and R. B. Smith (2017). “Subsurface imaging of the

Upper Geyser basin in Yellowstone using a large-N geophone array”, (submitted). 

ACKNOWLEDGMENTS

This research was supported by National Science Foundation (NSF) Grant Number CyberSEES-1442665, the King Abdullah University of Science and Technology (KAUST) under Award OCF-2014-CRG3-2300, and the U.S. Department of Energy, Geothermal Technologies Office, under Contract DE-EE0007080. Fieldwork for this project was partially supported by the Brinson Foundation and the Carrico Fund. The content of this article benefited from several informal conversations with Jonathan R. Delph and Keith D. Koper. Waveforms were pre-processed using the Seismic Analysis Code (SAC) software (Goldstein *et al.*, 2003; Goldstein and Snoke, 2005), and all figures presented were generated using the Generic Mapping Tool (GMT) software (Wessel *et al.*, 2013). The digital elevation model (DEM) in Figure 10a is based on services provided to the Plate Boundary Observatory (PBO) by National Center for Airborne Laser Mapping (NCALM; <http://www.ncalm.org>, last accessed May 2017). The PBO is operated by University NAVstar Consortium (UNAVCO) for EarthScope (<http://www.earthscope.org>, last accessed May 2017) and supported by the NSF (Number EAR-0350028 and EAR-0732947). The authors would specifically like to acknowledge Brandon Schmandt for proposing the nodal geophone deployment near Station NLU, Andy Trow for deploying the nodal stations as part of an undergraduate research project (UROP) supported by the University of Utah, Jamie Farrell for organizing the Old Faithful nodal deployment, and all involved with the Incorporated Research Institutions for Seismology (IRIS) Community Wavefield Experiment in Oklahoma. The authors would like to thank all of the faculty, Postdocs, and other students and staff responsible for deploying and maintaining the seismic stations used in this study. Finally, the authors would like to acknowledge the contribution of two anonymous reviewers and two journal editors, whose comments benefited the content of this article.

REFERENCES

- Ammon, C. J., G. E. Randall, and G. Zandt (1990). On the nonuniqueness of receiver function inversions, *J. Geophys. Res.* **95**, 15,303–15,318.
- Anderson, K., J. Sweet, and B. Woodward (2016). *IRIS Community Wavefield Experiment in Oklahoma, Incorporated Research Institutions for Seismology. Other/Seismic Network*, doi: [10.7914/SN/YW_2016](https://doi.org/10.7914/SN/YW_2016).
- Beck, S. L., and G. Zandt (2002). The nature of orogenic crust in the central Andes, *J. Geophys. Res.* **107**, 2230.
- Chen, C. W., D. E. Miller, H. A. Djikpesse, J. B. U. Haldorsen, and S. Rondenay (2010). Array-conditioned deconvolution of multiple-component teleseismic recordings, *Geophys. J. Int.* **182**, 967–976.
- Chu, R., D. V. Helmberger, D. Sun, J. M. Jackson, and L. Zhu (2010). Mushy magma beneath Yellowstone, *Geophys. Res. Lett.* **37**, L01306, doi: [10.1029/2009GL041656](https://doi.org/10.1029/2009GL041656).
- Clayton, R. W., and R. A. Wiggins (1976). Source shape estimation and deconvolution of teleseismic body waves, *Geophys. J. Roy. Astron. Soc.* **47**, 151–177.
- Crotwell, H. P., and T. J. Owens (2005). Automated receiver function processing, *Seismol. Res. Lett.* **76**, no. 6, 702–709.
- Delph, J. R., K. M. Ward, G. Zandt, M. N. Ducea, and S. L. Beck (2017). Imaging a magma plumbing system from MASH zone to magma reservoir, *Earth Planet. Sci. Lett.* **457**, 313–324.
- Dueker, K. D., and A. F. Sheehan (1997). Mantle discontinuity structure from midpoint stacks of converted *P* to *S* waves across the Yellowstone hotspot track, *J. Geophys. Res.* **102**, 8313–8327.
- Frassetto, A., G. Zandt, H. Gilbert, T. J. Owens, and C. H. Jones (2010). Improved imaging with phase-weighted common conversion point stacks of receiver functions, *Geophys. J. Int.* **182**, 368–374.
- Gans, C. R., S. L. Beck, G. Zandt, H. Gilbert, P. Alvarado, M. Anderson, and L. Linkimer (2011). Continental and oceanic crustal structure of the Pampean flat slab region, western Argentina, using receiver function analysis: New high-resolution results, *Geophys. J. Int.* **186**, 45–58.
- Goldstein, P., and A. Snoke (2005). SAC availability for the IRIS community, *Incorporated Institutions for Seismology Data Management Center Electronic Newsletter 1*, available at <http://ds.iris.edu/ds/newsletter/vol7/no1/193/sac-availability-for-the-iris-community/> (last accessed February 2017).
- Goldstein, P., D. Dodge, M. Firpo, and L. Minner (2003). SAC2000: Signal processing and analysis tools for seismologists and engineers, in *Invited Contribution to “The LASPEI International Handbook of Earthquake and Engineering Seismology”*, W. H. K. Lee, H. Kanamori, P. C. Jennings, and C. Kisslinger (Editors), Academic Press, London, United Kingdom.
- Hansen, S. M., and B. Schmandt (2015). Automated detection and location of microseismicity at Mount St. Helens with a Large-N geophone array, *J. Geophys. Res.* **52**, 7390–7397.
- Huang, H. H., F. C. Lin, B. Schmandt, J. Farrell, R. B. Smith, and V. C. Tsai (2015). The Yellowstone magmatic system from the mantle plume to the upper crust, *Science* **348**, 773–776.
- Inbal, A., J. P. Ampuero, and R. W. Clayton (2016). Localized seismic deformation in the upper mantle revealed by dense seismic arrays, *Science* **354**, 88–92.
- Incorporated Research Institutions for Seismology Data Management Center (IRIS-DMC) (2010). *Data Services Products: EARS EarthScope Automated Receiver Survey*, doi: [10.17611/DP/EARS.1](https://doi.org/10.17611/DP/EARS.1).
- Jones, C. H., and R. A. Phinney (1998). Seismic structure of the lithosphere from teleseismic converted arrivals observed at small arrays in the southern Sierra Nevada and vicinity, California, *J. Geophys. Res.* **103**, 10,065–10,090.
- Julia, J., C. J. Ammon, R. B. Herrmann, and A. M. Correig (2000). Joint inversion of receiver function and surface wave dispersion observations, *Geophys. J. Int.* **143**, 99–112.
- Kolb, J., and V. Lekić (2014). Receiver function deconvolution using transdimensional hierarchical Bayesian inference, *Geophys. J. Int.* **197**, no. 3, 1719–1735.
- Langston, C. A. (1979). Structure under Mount Rainier, Washington, inferred from teleseismic body waves, *J. Geophys. Res.* **84**, 4749–4762.
- Ligorria, J. P., and C. J. Ammon (1999). Iterative deconvolution and receiver-function estimation, *Bull. Seismol. Soc. Am.* **89**, no. 5, 1395–1400.
- Lin, F., D. Li, R. W. Clayton, and D. Hollis (2013). High-resolution 3D shallow crustal structure in Long Beach, California: Application of ambient noise tomography on a dense seismic array, *Geophysics* **78**, Q45–Q56.
- Ma, Y., and R. Clayton (2016). Structure of the Los Angeles basin from ambient noise and receiver functions, *Geophys. J. Int.* **206**, 1645–1651.
- Neal, S. L., and G. L. Pavlis (1999). Imaging *P* to *S* conversions with multichannel receiver functions, *Geophys. Res. Lett.* **26**, 2581–2584.
- Niu, F., A. Levander, S. Ham, and M. Obayashi (2005). Mapping the subducting Pacific slab beneath southwest Japan with Hi-net receiver functions, *Earth Planet. Sci. Lett.* **239**, 9–17.
- Schmandt, B., and R. Clayton (2013). Analysis of teleseismic *P* waves with a 5200-station array in Long Beach, California: Evidence

- for an abrupt boundary to Inner Borderland rifting, *J. Geophys. Res.* **118**, 5320–5338.
- Schmandt, B., K. Dueker, E. Humphreys, and S. Hansen (2012). Hot mantle upwelling across the 660 beneath Yellowstone, *Earth Planet. Sci. Lett.* **331/332**, 224–236.
- Shen, W., M. Ritzwoller, and V. Schulte-Pelkum (2013). A 3-d model of the crust and uppermost mantle beneath the central and western U.S. by joint inversion of receiver functions and surface wave dispersion, *J. Geophys. Res.* **60**, 1–15.
- Stanciu, C. A., R. M. Russo, V. I. Mocanu, P. M. Bremner, S. Hongsre-sawat, M. E. Torpey, J. C. VanDecar, D. A. Foster, and J. A. Hole (2016). Crustal structure beneath the Blue Mountains terranes and cratonic North America, eastern Oregon, and Idaho, from teleseismic receiver functions, *J. Geophys. Res.* **121**, 5049–5067.
- Trabant, C., A. R. Hutko, M. Bahavar, R. Karstens, T. Ahern, and R. Aster (2012). Data products at the IRIS DMC: Stepping stones for research and other applications, *Seismol. Res. Lett.* **83**, no. 5, 846–854.
- University of Utah (1962). *University of Utah Regional Seismic Network, International Federation of Digital Seismograph Networks, Other/ Seismic Network*, doi: [10.7914/SN/UU](https://doi.org/10.7914/SN/UU).
- Ward, K. M., G. Zandt, S. L. Beck, D. H. Christensen, and H. McFarlin (2014). Seismic imaging of the magmatic underpinnings beneath the Altiplano–Puna volcanic complex from the joint inversion of surface wave dispersion and receiver functions, *Earth Planet. Sci. Lett.* **404**, 43–53.
- Wessel, P., W. H. F. Smith, R. Scharroo, J. F. Luis, and F. Wobbe (2013). Generic mapping tools: improved version released, *Eos Trans. AGU* **94**, 409–410.
- Wölbern, I., B. Heit, X. Yuan, G. Asch, R. Kind, J. Viramonte, S. Tawackoli, and H. Wilke (2009). Receiver function images from the Moho and the slab beneath the Altiplano and Puna plateaus in the central Andes, *Geophys. J. Int.* **177**, no. 1, 296–308.
- Yuan, X., J. Ni, R. Kind, J. Mechie, and E. Sandvol (1997). Lithospheric and upper mantle structure of southern Tibet from a seismological passive source experiment, *J. Geophys. Res.* **102**, no. B12, 27,491–27,500.
- Zhu, L. (2000). Crustal structure across the San Andreas fault, southern California from teleseismic converted waves, *Earth Planet. Sci. Lett.* **179**, 183–190.
- Zhu, L., and H. Kanamori (2000). Moho depth variation in southern California from teleseismic receiver functions, *J. Geophys. Res.* **105**, 2969–2980.

Kevin M. Ward
Fan-Chi Lin
Department of Geology and Geophysics
University of Utah
Frederick Albert Sutton Building
115 South 1460 East, Room 383
Salt Lake City, Utah 84112-0102 U.S.A.
kevin.m.ward@utah.edu

Published Online 9 August 2017